

# Electrical-Charge-Mediated Cancer Cell Targeting via Protein Corona-Decorated Superparamagnetic Nanoparticles in a Simulated Physiological Environment

Jian Zhao,<sup>\*,†,‡,⊥</sup> Shengming Wu,<sup>§,⊥</sup> Jingwen Qin,<sup>§</sup> Donglu Shi,<sup>\*,§,||</sup> and Yilong Wang<sup>\*,§</sup>

<sup>†</sup>School of Materials Science and Engineering, Qilu University of Technology (Shandong Academy of Sciences), Jinan 250353, China

<sup>‡</sup>Key Laboratory of Rubber-Plastics Ministry of Education/Shandong Provincial Key Laboratory of Rubber-Plastics, Qingdao University of Science & Technology, No. 53 Zhengzhou Road, Qingdao 266042, China

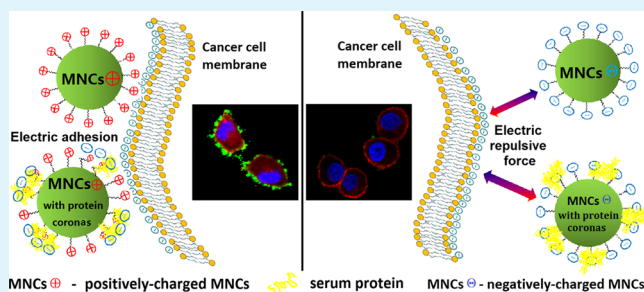
<sup>§</sup>The Institute for Translational Nanomedicine, Shanghai East Hospital, the Institute for Biomedical Engineering & Nano Science, Tongji University School of Medicine, Shanghai 200092, P. R. China

<sup>||</sup>The Materials Science and Engineering Program, College of Engineering and Applied Science, University of Cincinnati, Cincinnati, Ohio 45221, United States

## Supporting Information

**ABSTRACT:** A critical issue in nanomedicine is on the understanding of nano–bio interface behaviors, particularly when the nanoparticles are inevitably decorated by protein coronas in the physiological fluids. In this study, the effects of particle surface corona on cancer cell targeting were investigated in simulated physiological fluids. Cell targeting was achieved by two strategies: (1) using conventional epithelial cell adhesion molecule antibody-functionalized Fe<sub>3</sub>O<sub>4</sub> nanoparticles and (2) rendering the same but naked magnetic nanoparticles electrically positively charged, enabling them to electrostatically bind onto the negatively charged cancer cells. The cell–particle electrostatic binding was found to be much stronger with faster reaction kinetics than the immunological interactions even at 4 nC. Both types of nanoparticles were decorated with various protein coronas by administration in a simulated physiological system. Well-decorated by protein coronas, the electrically charged particles retained strong electrostatic interactions with cancer cells, even upon reversal of the particle zeta potential from positive to negative. This behavior was explained by a nonuniform corona modulation of the particle surface charge distributions, exposing locally positively charged regions, capable of strong electrostatic cell binding and magnetic capturing in a physiological environment. This fundamental discovery paves new way for sensitive detection of circulating tumor cells in whole blood in clinical settings.

**KEYWORDS:** nano–bio interface, protein corona, surface charged nanoprobe, cancer cell capture, superparamagnetic



## INTRODUCTION

In nanotechnology-based cancer diagnosis and therapeutics, the nanoparticle (NP) surface decoration by biological media plays a key role in all aspects of biomedical efficacy via a corona of biological macromolecules. While in chemical synthesis, the structure and surface functional groups of the NPs are seen to be the key material components, the situation is drastically changed as the NPs are dispersed in the physiological media (for instance, human serum) and subsequently developing the so-called “protein corona”. In other words, NPs undergo significant “identity change” once dispersed in biological fluids, by taking up complex proteins on their surfaces, rendering them “unrecognizable” compared to the bare particles.<sup>1</sup> In this fashion, the biochemical–physical properties of the NPs will be severely altered, in turn affecting cell targeting, systemic circulation, fibrillation, cellular uptake,

and biocompatibility.<sup>2–7</sup> The transformed NPs, through complex surface proteins, comprise a new clustering structure, termed as “protein corona,” that is distinctively different from the original as-synthesized particles.<sup>8,9</sup> In nanomedicine, it is in fact the protein coronas, rather than bare NPs, that interface with the biological systems, such as cells, with unique behaviors and mechanisms.

Therefore, the biomedical applications of NPs are complicated by the dynamic physiochemical conditions in serum environment, especially when encountering a large number of proteins. One major issue deals with the in vivo fate of exogenous NPs by opsonization and phagocytosis via

**Received:** September 1, 2018

**Accepted:** November 14, 2018

**Published:** November 14, 2018

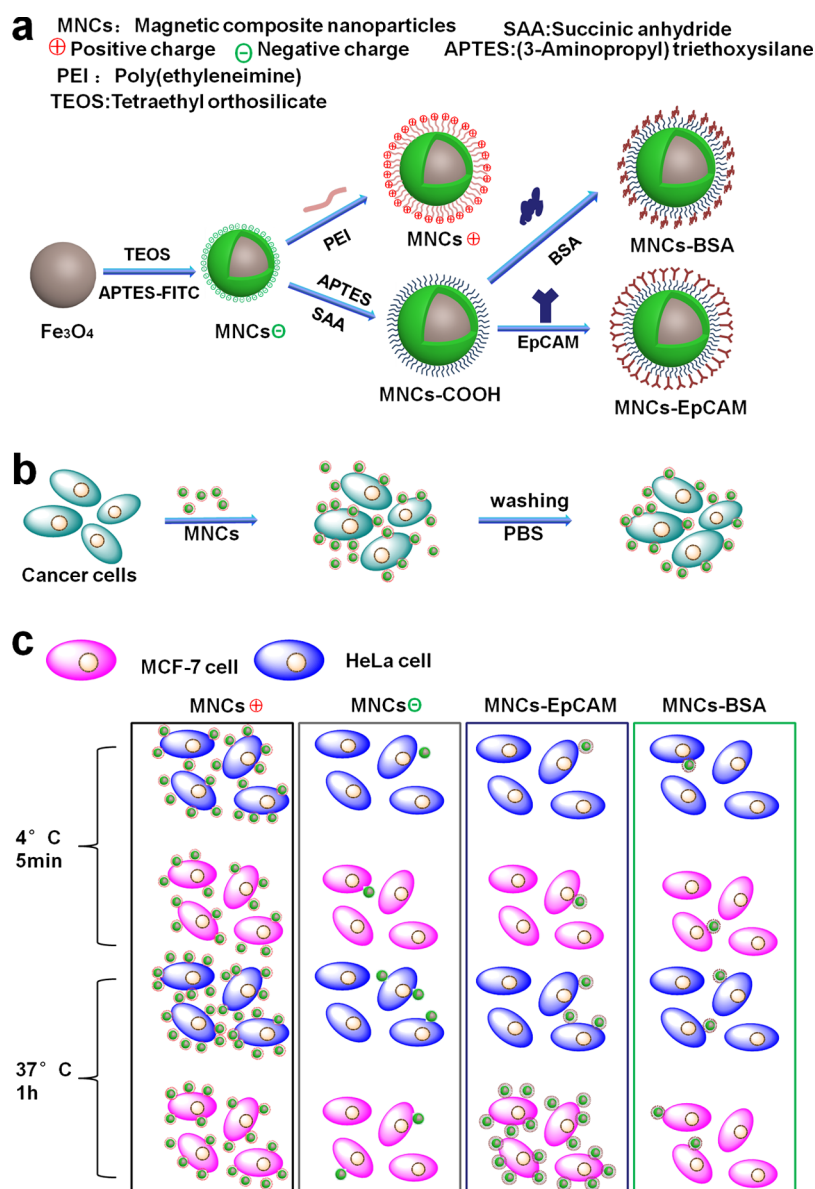


**Figure 1.** Schematic illustrations of synthetic pathways of the four kinds of different MNCs (a) and their binding to MCF-7 and HeLa cells at different incubation conditions (b,c).

reticuloendothelial system's (RES) protagonists.<sup>10</sup> It has been shown that the negatively or positively charged polymeric NPs are prone to phagocytosis by macrophages as compared to neutral NPs.<sup>11,12</sup> The surface charges can even render the NPs stealth in bloodstream, while having strong effects on their cellular interaction, internalization, and biodistribution.<sup>13–15</sup> To reduce interference from blood stream, the pH-sensitive surface charge reversible nanosystems have been developed for effective cancer therapy.<sup>16–18</sup> Caruso et al. studied the antibody-conjugated microspheres via protein adsorption and found no adverse effects on cancer cell targeting ability upon corona formation.<sup>19</sup>

In cancer theranostics, cell targeting has been the key in spatial and temporal control of optimum efficacy. The current targeting strategy has been primarily focused on the biomarker-based “ligand–receptor” reaction mechanism.<sup>20</sup> With this approach, a variety of nanoprobe has been designed and developed, exhibiting significant affinity to cancer cells upon surface functionalization and conjugation with various

biomarkers.<sup>21–23</sup> Although considerable progress has been made via these nanoprobe, the main problem remains that is associated with the molecular similarities not only between cancer and normal cells, but also within the same cancer cell lines. This is a fundamental biological barrier that cannot be easily overcome because of the genetic nature of cancers.<sup>24</sup> Furthermore, nonspecific binding has been another challenge in biomarker-based cell targeting. In recent years, the morphological and biomechanical features of cancer cells, such as size and stiffness, have been utilized to distinguish between the cancer and normal cells, particularly in detection of the circulating tumor cells (CTC), but its success has been hindered by limited sensitivity and efficiency.<sup>25,26</sup>

To address these critical issues, a new approach has emerged based on the cancer cell surface negative charges, a universal biophysical property of all cancer cells, regardless of their phenotypical and molecular differences.<sup>27</sup> The core concept of charge-based targeting originates from the “Warburg effect,” a hallmark metabolic pattern shared by all cancer cells.<sup>28–30</sup> In a

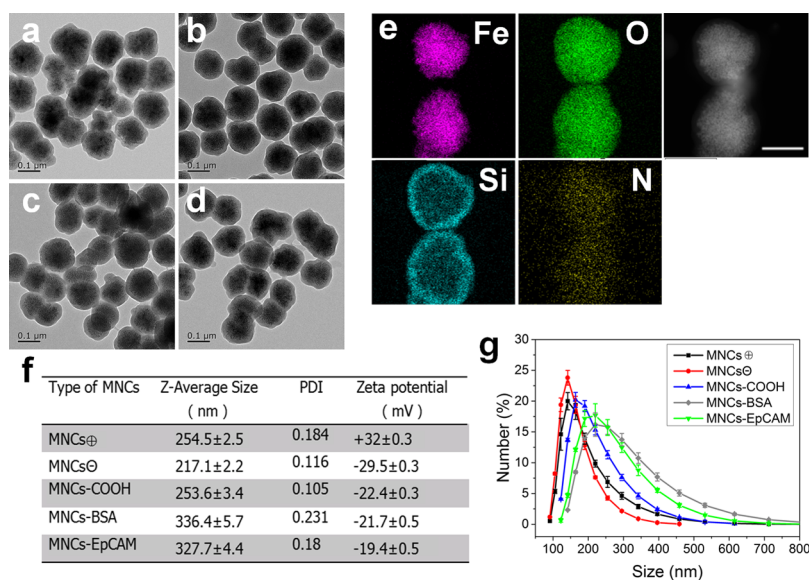


**Figure 2.** Physicochemical properties of the functionalized MNC particles. Transmission electronic microscopy (TEM) images of (a) MNCs $\oplus$ , (b) MNCs $\ominus$ , (c) MNCs-BSA, (d) MNCs-EpCAM; (e) high-angle annular dark-field scanning TEM (HAADF-STEM) image of MNCs $\oplus$  and elemental mapping for Fe, Si, O, and N; (f) dynamic light scattering (DLS) sizes and zeta potentials of MNCs in aqueous solution, and (g) DLS histogram showing the hydrodynamic size distributions of MNCs. The scale bars of a–e are all 100 nm.

normal cell, mitochondria, as a “power house,” converts glucose to adenosine triphosphate (ATP) via the tricarboxylic acid (TCA) cycle. However, the metabolic mechanism of cancer cells is fundamentally different by glycolysis, even in the presence of sufficient oxygen. Cancer cells characteristically secrete a large amount of lactate acid via consumption of glucose, responsible for major cancer cell metabolism. Consequently, the transportation of lactate from the cytoplasm will inevitably remove positive ions, such as Na<sup>+</sup> and K<sup>+</sup>, to form lactic salts, generating a net of negative charges on cancer cell surfaces. The negative cancer cell surface charges are therefore the biophysical (or bioelectrical) manifestation of the Warburg effect. The negative charges on the surfaces of cancer cells are found to be proportional to the rate of glycolysis.<sup>27</sup> It is the perpetuating motion of anions, associated with lactate secretion, that are responsible for the negative cancer cell surface electrical charges. The charge-based cell targeting is accomplished by rendering the Fe<sub>3</sub>O<sub>4</sub> NPs electrically positive, via poly(ethyleneimine) (PEI)-surface functionalization, and enabling them to massively bind onto the negatively charged cancer cell surfaces. Because of the superparamagnetic nature of Fe<sub>3</sub>O<sub>4</sub>, the cancer cells, surface-bound by numerous charged-NPs, can be magnetically separated, and even killed *in situ* by various means such as the photothermal effect.<sup>31</sup>

Although cancer microenvironment has been extensively studied in terms of the “Warburg effect,” it remains unknown how cancer cells electrostatically respond to the charged nanoprobes in terms of interaction strength, binding mechanism, and charge distribution, especially in comparison to the biomarker-based cell targeting. Fundamentally more important is the fact that upon developing the “protein corona” on the NP surfaces in a physiological fluid, charge redistribution will take place and significantly affect the zeta potential, thereby changing the electrostatic cell binding capability of the NPs. Technically, the NP surfaces can be modified by either conjugating with ligand receptors for marker-based or electrically charged polymers for charge-based cancer cell targeting and binding. A combination of both is also

possible by surface engineering of a “charged corona” that can, to a large extent, modulate the surface charges in both magnitude and sign in a wide range. With both charge- and marker-based cell targeting mechanisms, it is possible to investigate their differences and form deep insights into binding mechanism, temperature dependence, reaction kinetics, and charge distributions on cells. This can be done by comparative experiments with either charge or biomarker, which will result in different binding strengths under given conditions. It is also possible to modulate the surface electrical charges by different protein coronas and study the consequent cell binding variations.

In this study, we carried out comparative parallel experiments on both receptor–ligand and electrical-charge-mediated cell targeting using two epithelial cancer cell lines: MCF-7 and HeLa. The former is epithelial cell adhesion molecule (EpCAM) antigen-overexpressed, while the latter is not. The anti-EpCAM antibody is typically used to conjugate with NPs for specifically targeting the EpCAM antigen-overexpressed cells. Comparative experiments between the biomarker- and charge-based cell targeting were performed by using superparamagnetic Fe<sub>3</sub>O<sub>4</sub> NPs with different surface functional groups. We also investigated the effects of protein coronas on cancer cell binding by the magnetic nanocomposites (MNCs).

As schematically shown in Figure 1a, MNCs are structurally composed of a Fe<sub>3</sub>O<sub>4</sub> core and a silica shell with fluorescein isothiocyanate (FITC) fluorescence, synthesized by the hydrothermal and sol–gel reaction, respectively.<sup>31,32</sup> MNCs are rendered negatively charged by surface functionalization with the abundant hydroxyl groups, forming a composite of Fe<sub>3</sub>O<sub>4</sub>@silica, denoted as MNCs $\ominus$ . The positively-charged Fe<sub>3</sub>O<sub>4</sub>@silica [positively-charged MNCs (MNCs $\oplus$ )] is achieved by PEI surface modification through electrostatic interactions between the hydroxyl and imine groups.

As also shown in Figure 1a, MNCs–EpCAM, and its control MNCs–bovine serum albumin (BSA), can be developed by respectively conjugating COOH-MNCs with anti-EpCAM antibody (MNCs–EpCAM) and BSA (MNCs–BSA). The

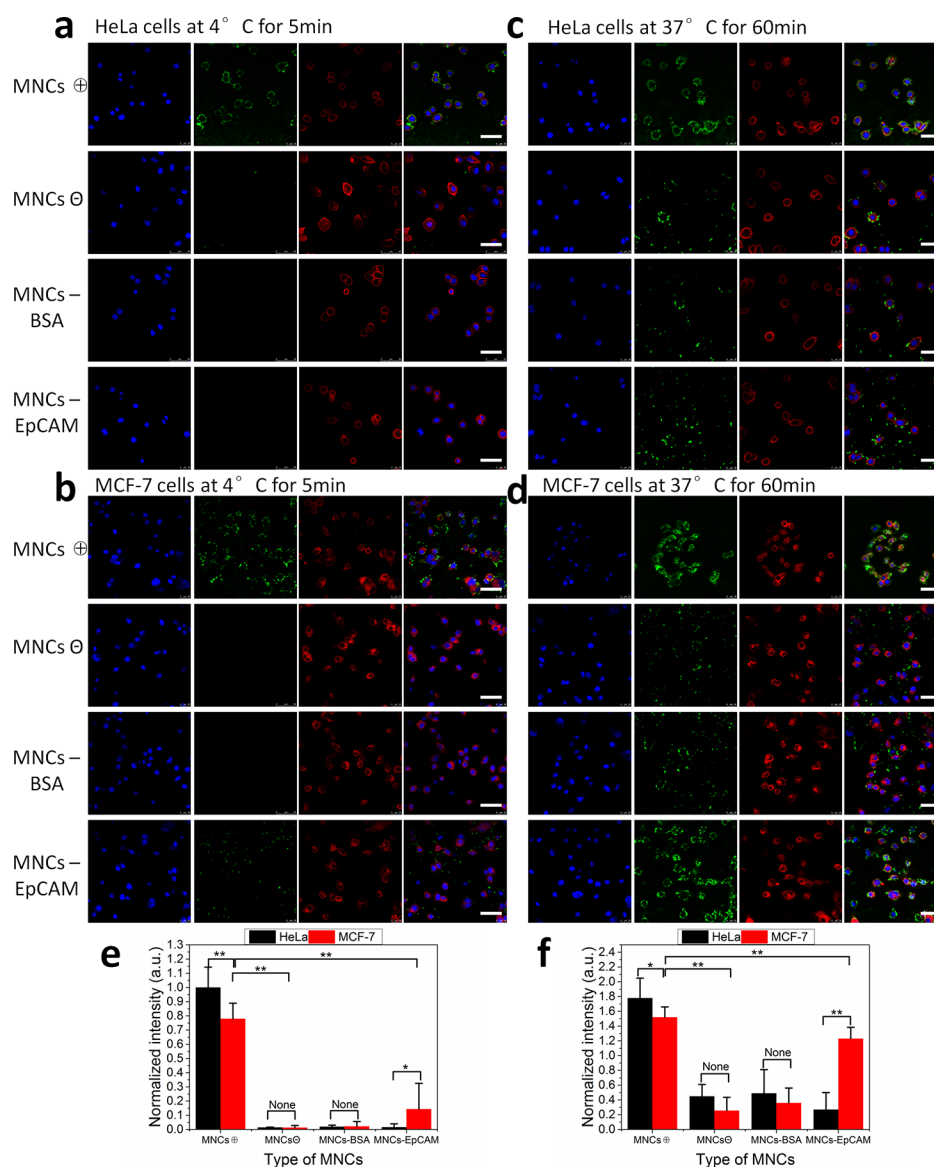


**Figure 3.** Fluorescence Confocal images showing the HeLa and MCF-7 cells treated with four different kinds of MNCs under different incubation conditions, respectively: (a,b) at 4 °C for 5 min, (c,d) at 37 °C for 60 min in a serum-free medium. All samples were washed three times with PBS (pH 7.4) to remove the extra MNCs. The scale bars are all 50  $\mu$ m. Quantitative ratios of the green fluorescence intensities on the membranes of HeLa and MCF-7 cells incubated with different MNCs, analyzed by ImageJ software and 50 cells, were measured as shown in panels a–d. The normalized fluorescent intensity of (e) HeLa and MCF-7 cells incubated with different MNCs at 4 °C for 5 min, and (f) HeLa and MCF-7 cells incubated with different MNCs at 37 °C for 60 min. The fluorescence intensity is set as 1.0 for HeLa cells incubated with MNCs $\oplus$  at 4 °C for 5 min.

typical process of cell binding is through mixing cancer cells with MNCs and washing with phosphate-buffered saline (PBS) (Figure 1b). Figure 1c shows binding efficiencies resulting from different MNCs (i.e., MNCs $\oplus$ , MNCs $\ominus$ , MNCs–EpCAM, and MNCs–BSA) at different incubation temperatures and times (4 °C for 5 min and 37 °C for 60 min). Note that all MNCs with different surface functionalizations have a similar average diameter of 120 nm. The representative experimental results of this study are schematically depicted in Figure 1c. As can be seen from Figure 1c, the MNCs $\oplus$  result in the most efficient cell binding for both HeLa and MCF-7 cell lines at 4 °C and 37 °C, respectively, while that of which is significantly weakened for the negatively-charged MNCs (MNCs $\ominus$ ), indicating that all cancer cells are negatively charged. In the parallel study using biomarker-

based targeting, one can see that the strongest binding takes place, at 37 °C, for the MCF-7 cell line using overexpressed MNCs–EpCAM, while that of the HeLa cells exhibits insignificant cell binding. Weak cell binding is also observed using the control of MNCs–BSA. The detailed experimental results consistent with Figure 1 are shown and discussed in the following sections.

## RESULTS AND DISCUSSION

The morphological and physiochemical properties of the MNCs are shown in Figure 2. As can be seen in this figure, MNCs with different surface charges and functional groups exhibit similar shape, size, and dispersity. Most of them are morphologically spherical with a TEM size of 120 nm (Figure 2a–2d). The Z-average hydrodynamic diameters of the

positively charged ( $254.5 \pm 2.5$  nm), negatively charged ( $217.1 \pm 2.2$  nm), and carboxylic acid-functionalized MNCs ( $253.6 \pm 3.4$  nm) are quite similar, as shown in Figure 2f. The polydispersity indexes are also similar among these particles (Figure 2f). Zeta potentials of the positively charged, negatively charged, and carboxylic-acid-functionalized MNCs are +32, -29.5, and -22.4 mV, respectively [MNCs were dispersed in deionized water (DIW), pH 7.4, Figure 2f]. The number versus size statistical curves exhibit rather sharp peaks of various MNCs, indicating their good dispersities in aqueous solution (Figure 2g). Figure S1 shows the cell viability of HeLa and MCF-7 cells treated by positively and negatively charged and carboxylic group-functionalized magnetic NPs. The positively charged NPs exhibit only slightly higher cytotoxicity, but none to HeLa and MCF-7 cells at the working concentration.

Upon antibody conjugation, the hydrodynamic diameters of carboxylic-acid-functionalized MNCs significantly increase as expected. The Z-average diameters of BSA- and anti-EpCAM antibody-conjugated MNCs are, respectively,  $336.4 \pm 5.7$  and  $327.7 \pm 4.4$  nm, with corresponding zeta potentials of -21.7 and -19.4 mV. The number versus size statistical curves of these particles exhibit wider peaks but still with good colloidal stability (Figure 2g). Figure S2a–c shows fluorescent microscopy images of the FITC-labeled MNCs with the positive and negative surface charges and the surface carboxylic acid groups. As can be seen in Figure S2d, they all exhibit strong green fluorescence and retain the same intensities after incubation in Dulbecco's modified Eagle's medium (DMEM) media for 24 h. Conjugation of anti-EpCAM antibody onto COOH-MNCs was confirmed by using the lateral flow strips with rabbit-anti-mouse IgG protein on C-line (Figure S3). In this experiment, the MNC aqueous solution ( $2 \mu\text{g}$  of MNCs) was dipped onto the binding pad of the strip, and it permeated through the strips. As can be seen in this figure, only the anti-EpCAM-antibody-conjugated MNCs result in a brown band on C-line because of immunological reactions between anti-EpCAM antibody and IgG protein (Figure S3a). In contrast, no reactions take place for pure COOH-MNCs and the BSA-conjugated COOH-MNCs (Figure S3b,c). These results validate successful conjugation and well-retained antibody activities.

Figure 3 shows binding efficiencies of HeLa and MCF-7 cells by the MNCs with different surface structures and FITC labeling at incubation conditions indicated. These NPs include MNCs $\oplus$ , MNCs $\ominus$ , BSA-conjugated MNCs (BSA-MNCs), and anti-EpCAM antibody-conjugated MNCs (EpCAM-MNCs). All were incubated with HeLa and MCF-7 cells under a given condition. To avoid endocytosis of MNCs by cancer cells, the incubation condition was set at 4 °C for 5 min.<sup>27</sup> However, for antibody-antigen-driven interaction, incubation at 37 °C for 60 min was preferred considering its slower reaction kinetics.

As shown in Figure 3a, the nucleus was stained by 4',6-diamidino-2-phenylindole (DAPI), and the cytoplasm was stained by rhodamine-phalloidin. Among different MNCs, incubated with HeLa cells at 4 °C for 5 min, only the MNCs $\oplus$  significantly bind onto cancer cell membranes in large quantities, exhibiting strong green fluorescence of FITC. Under the same condition, however, very weak fluorescence can be observed when incubated with MNCs $\ominus$  and anti-EpCAM- or BSA-conjugated MNCs, indicating insignificant binding (Figure 3a). Similar results are found for MCF-7 cells

as shown in Figure 3b. Consistently, only the MNCs $\oplus$  strongly bind onto MCF-7 cells as expected because of opposite charges between the MNCs (positive) and cancer cells (negative). Also, anti-EpCAM antibody-conjugated MNCs can also interact with MCF-7 cells to some extent because of their comparatively high EpCAM expression.

Antibody-antigen interaction-mediated cell binding is considerably enhanced when incubation takes place at 37 °C for 60 min, as shown in Figure 3c,d. Again, the MNCs $\oplus$  show the brightest green fluorescence due to electrostatic binding, while the signals appear to be increasingly stronger for anti-EpCAM or BSA-conjugated MNCs, for both HeLa and MCF-7 cell lines (Figure 3c,d). On the basis of the results shown in Figure 3 and schematically depicted in Figure 1, it can be concluded that the electrostatic cell binding strength is much stronger than those by antibody reactions at the same incubation condition. It was noted that the fluorescent signal appears stronger for the anti-EpCAM-antibody-conjugated MNCs with MCF-7 cells over HeLa cells because EpCAM antigen is overexpressed in the MCF-7 cell line.

For a more straightforward comparison, ImageJ software was applied to analyze the fluorescence signals of all samples shown in Figure 3a–d. Figure 3e shows the comparison of the fluorescence intensity of each sample to that from incubating HeLa cells with the MNCs $\oplus$  at 4 °C for 5 min. At 4 °C for 5 min, the fluorescence intensity from the positive MNCs (black) is much higher than that of the EpCAM conjugated, indicating that electrostatic binding is much more efficient. Similar fluorescent intensity difference is seen for the MCF-7 cells (Figure 3e). At the incubation condition of 37 °C for 60 min, as shown in Figure 3f, the MCF-7 cells exhibit comparable signals for both MNCs $\oplus$  and the anti-EpCAM-antibody-conjugated MNCs. At elevated temperatures for a prolonged time, the antibody-antigen reaction becomes more complete, resulting in improved cell binding.

Figure S4 shows the fluorescence confocal images of HeLa and MCF-7 cells after incubation with MNCs labeled with FITC. In Figure S4a, at 4 °C for 5 min, the FITC labeled MNCs $\oplus$  uniformly surround the membranes of HeLa and MCF-7 cells, indicating strong binding, but without any endocytosis. The blue islands are the nuclei inside HeLa and MCF-7 cells. For MNCs $\ominus$ , however, no cell binding takes place and therefore are absent of any fluorescent signals in both HeLa and MCF-7 cells. The situation is drastically different under the condition of 37 °C for 60 min as shown in Figure S4b. As can be seen in this figure, the NP binding appears to be diffused for HeLa cells when conjugated with anti-EpCAM or BSA, which is consistent with underexpressed EpCAM antigen in this cell line. Because of EpCAM antigen overexpression in MCF-7 cells, EpCAM-MNCs result in considerably improved cell binding. The fluorescence signal from BSA-MNCs is associated with nonspecific adsorption between the MNCs and cells. These results provided direct experimental evidence that the electrostatic interfacial interaction is strong.

To further investigate reaction kinetics, cell binding was performed at 4 °C with different incubation times at 10 s, 10 min, 30 min, and 60 min, using the same MNC concentration. Figure S5 shows the fluorescence microscopy images of HeLa cells bound with MNCs $\oplus$  (Figure S5a) and MNCs $\ominus$  (Figure S5b) for different incubation times. As can be seen in Figure S5a, the fluorescence intensity consistently increases with increasing time up to 60 min, indicating more and more

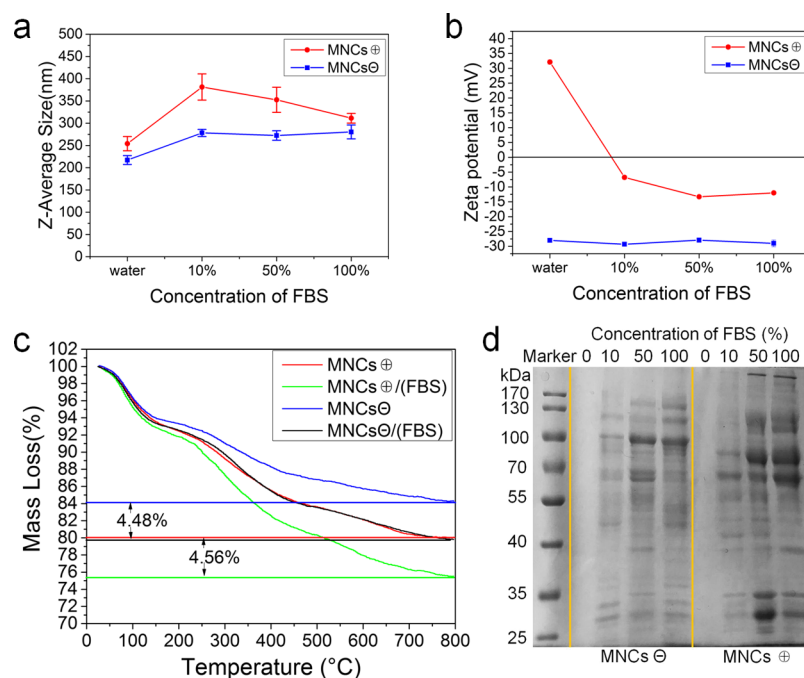


**Figure 4.** Physicochemical properties of surface-charged MNCs treated by FBS proteins. After incubation of MNCs with FBS solution, extra FBS was washed away by three-times of magnetic separation and redispersion. (a) DLS sizes and (b) corresponding zeta potentials of MNCs $\oplus$  and MNCs $\ominus$ , after treating by DMEM solution of FBS at different concentrations: 0, 10, 50, and 100 v/v %. (c) TG curves of MNCs $\oplus$  and MNCs $\ominus$  and corresponding products after treatment by FBS at a concentration of 100%. (d) Sodium dodecyl sulfate-polyacrylamide gel electrophoresis (SDS-PAGE) image of surface-charged MNCs following incubation at 25 °C for 1 hour in DMEM medium containing FBS at varying concentrations: 0, 10, 50, 100 v/v %. Reference bands associated with particular molecular weights are displayed by a marker in the left of the image.

MNCs binding onto the cell surfaces. For MNCs $\ominus$ , however, the fluorescence signal is rather weak even at prolonged incubation times. Figure S5c shows quantitative data of relative ratios of the fluorescent signals from Figure S5a,b. As shown in Figure S5c, HeLa cells exhibit a strong fluorescence signal that rapidly increases to  $\sim 1.1$  at 5 min, thereafter reaching a plateau up to 60 min. The fluorescent signal remains rather low for the entire incubation time period for the MNCs $\ominus$ . The fluorescence intensity from the cells incubated with the MNCs $\oplus$  at 4 °C for 5 min was set as 1.0 for both curves shown in Figure S5c, and analyzed by using ImageJ software. According to the quantitative data shown in Figure S5c, there is only a slight increase of the fluorescence intensity ratio from 0 to 0.2 for MNCs $\ominus$ . In contrast, the fluorescence intensity ratio of MNCs $\oplus$  has increased from 0.2 to 1.4 at 30 min and remained at the same level up to 60 min. Figure S5d,e shows the fluorescence confocal images of HeLa cells bound with both MNCs $\oplus$  and MNCs $\ominus$ , respectively. Note that in these figures, the cell nucleus is stained by DAPI (blue) and membrane by rhodamine-phalloidin (red). As can be clearly seen in Figure S5d, the positively charged NPs uniformly bind on the cell membranes without endocytosis. The co-localization of the red and green fluorescence indicates the binding site of MNCs $\oplus$  on the cell membrane. However, the green fluorescence is absent for the negatively charged NPs as shown in Figure S5e. These are the strong experimental evidences that the cancer cells are negatively charged and therefore are attractive when encountering MNCs $\oplus$ , while repulsive in the vicinity of MNCs $\ominus$ .

Although the charge-driven cell binding is shown to be effective in vitro, the NP surface electrical changes will be modified by protein corona in a physiological environment,

such as blood plasma. It is important, therefore, to investigate cell binding and surface behaviors of NPs in various physiological fluids. For this purpose, the surface-charged MNCs were incubated with HeLa cells at 4 °C for 5 min after incubation in aqueous solutions containing fetal bovine serum (FBS) concentrations of 0, 10, 50, and 100 v/v % for 1 h. The “hard” protein corona-coated MNCs are defined as those MNCs whose extra FBS has been, upon incubation, removed by three-time washing. The “soft” protein corona-coated MNCs refer to those without the washing process. The “soft” corona can be obtained by adding FBS when incubating cancer cells with the surface-charged MNCs.<sup>33</sup>

The physicochemical properties of MNCs with “hard” protein corona are shown in Figure 4. As shown in Figure 4a, zeta potential of the MNCs $\oplus$  is initially positive in the absence of FBS (+30 mV at 0%), but rapidly decreases to  $-7.3$ ,  $-14.0$ , and  $-12.0$  mV at FBS concentrations of 10, 50, and 100 v/v %, respectively. The hydrodynamic diameter of the MNCs $\oplus$ , with “hard” protein corona, increases to about 400 nm. Zeta potentials of the MNCs $\ominus$  remain negative and more or less unchanged in a wide FBS concentration range (0–100%), with some surface adsorbed protein due to the positively charged surface patches (Figure 4a).<sup>34</sup>

The amount of “hard” protein corona on the surface-charged MNCs was determined by thermogravimetric (TG) analysis before and after treatment with FBS solution. As shown in Figure 4b, the mass losses of 4.48 and 4.56%, respectively, correspond to the “hard” protein coronas on the MNCs $\ominus$  and MNCs $\oplus$ . Mass loss (4.48%) is in fact the fraction of polycation polymer from MNCs $\oplus$ . The protein adsorbed on the surfaces of surface-charged MNCs was directly observed by characterization of SDS-PAGE. According to the reference

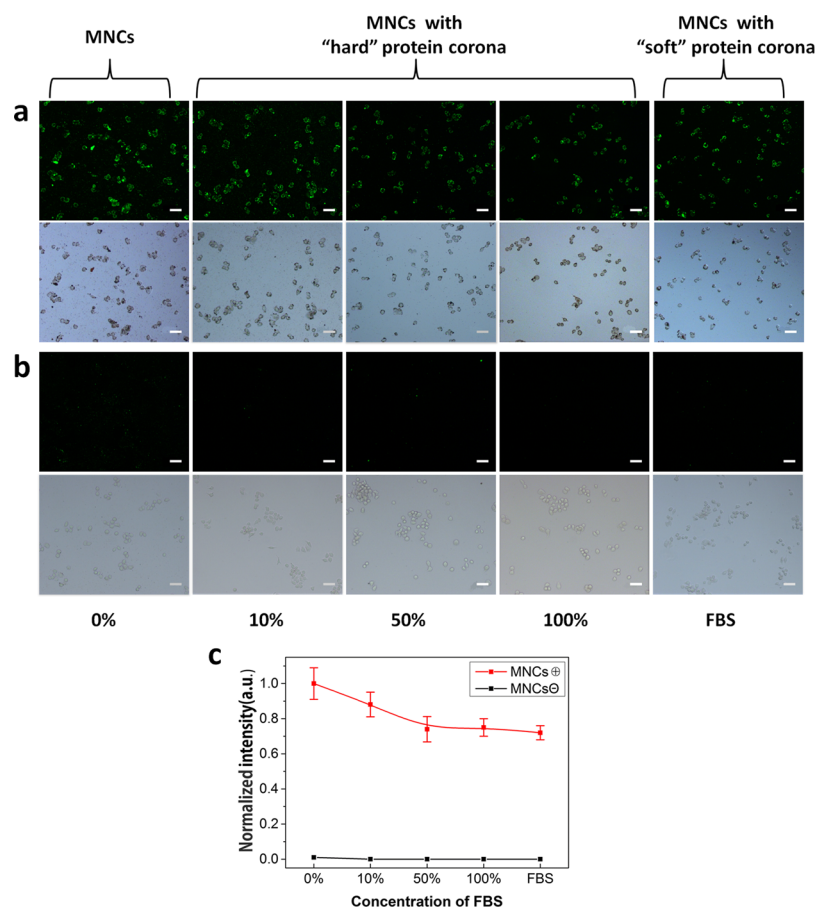


**Figure 5.** Fluorescence microscopy images of HeLa cells incubated with (a) MNCs $\oplus$  and (b) MNCs $\ominus$  including the “hard” or “soft” protein corona-coated MNCs. The corona-decorated MNCs were obtained by treating with FBS aqueous solutions containing FBS at the concentrations 0, 10, 50, and 100 v/v %. (c) Quantitative fluorescence intensities of cancer cells corresponding to the images in panels a and b, analyzed by ImageJ software. The fluorescence intensity of HeLa cells bound with MNCs $\oplus$  without FBS treatment is set as the reference intensity. The curves represent the relative fluorescence intensity ratios of cancer cells bound with the “hard” and “soft” protein corona-decorated MNCs. All scale bars are 100  $\mu\text{m}$ .

bands (marker) on the left-side in Figure 4c, abundant protein molecules with different molecular weights (from 30 to 130 kDa) are adsorbed by the MNCs $\oplus$  and MNCs $\ominus$ , thus forming the protein coronas. The adsorbed protein on the surface-charged MNCs is similar to those with 50 and 100 v/v % FBS concentrations, significantly higher than that of 10%. Although the protein coronas adsorbed on the MNCs with different surface charges are similar, which have been reported for the Au NPs–protein interaction,<sup>35</sup> as shown in Figure 4d, the molecular weights of the adsorbed proteins are considerably different between the MNCs $\oplus$  and MNCs $\ominus$ . The compositions of the adsorbed protein coronas on the differently charged MNCs, treated by 100 v/v % FBS, were characterized by liquid chromatography–mass spectrometry (LC–MS) analysis. The protein coronas were first released from MNCs and treated by gel electrophoresis. Protein bands were excised from the gel, subjected to in situ hydrolysis, and analyzed by MS. Table S1 lists the major parts of proteins adsorbed on the surfaces of the MNCs treated by FBS, followed by three-time washing. As shown in this table, different proteins are identified from coronas on the MNCs $\oplus$  or MNCs $\ominus$ . As shown in this table, 57 proteins are common types on MNCs of both charge signs (Table S1, pink), 23 proteins exclusively present on the MNCs $\oplus$  (Table S1, green), and 19 only on the MNCs $\ominus$  (Table S1, purple). According to the results of SDS-PAGE and

LC–MS, albumin and heat shock proteins are responsible for the intense bands of protein adsorbed on the surfaces of the positively charged magnetic NPs treated by 100% FBS with 65 and 84 kDa molecular weight. The results indicated the actual protein coronas decorated on MNCs, therefore, exerts strong effects on the MNCs’ charge reversal. In this fashion, the adsorbed proteins on the charged MNCs play a key role in the charge-based cancer cell targeting.

Figure 5 shows the fluorescence microscopy images of HeLa cells incubated with surface-charged MNCs treated by FBS of different concentrations at 4 °C for 5 min. In the entire range of 0–100% FBS, as shown in Figure 5a, the positive MNCs display the strongest fluorescence signal compared to those of the MNCs $\ominus$  (Figure 5b). These results clearly show significant electrostatic interaction responsible for efficient cancer cell binding by the MNCs $\oplus$ . The binding efficiency of the MNCs $\oplus$ , however, decreases with increasing FBS concentration, as a result of “hard” protein corona formation on NP surfaces.

For “soft” protein corona, the fluorescence microscopy images of the HeLa cells are bound with MNCs $\oplus$  (Figure 5a) and MNCs $\ominus$  (Figure 5b) in the presence of free FBS and shown in Figure 5 (marked as “MNCs with ‘soft’ protein coronas”). Upon incubation of MNCs with cancer cells in the presence of FBS, proteins tend to adsorb onto the surfaces of

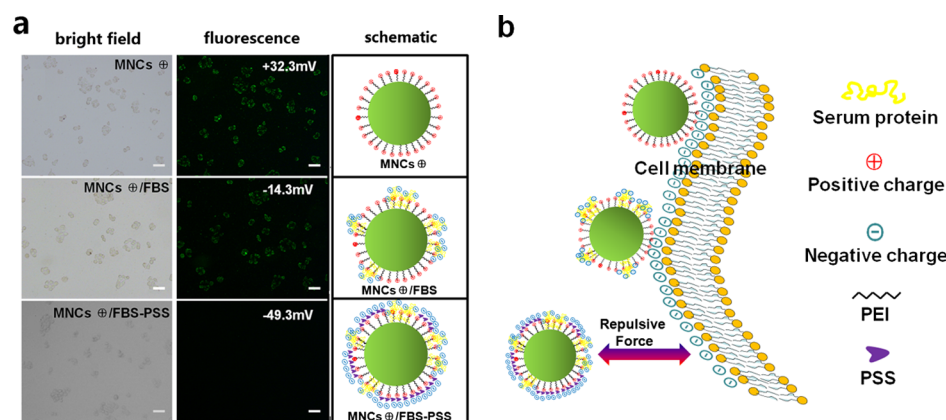


**Figure 6.** Fluorescence microscopy images of HeLa cells incubated with different MNCs: (a) bright-field images (left column), fluorescence microscopy images (middle column), and schematics (right column) of the MNCs $\oplus$ , 100% FBS-treated MNCs $\oplus$  (MNCs $\oplus$ /FBS), and PSS-treated MNCs $\oplus$ /FBS (MNCs $\oplus$ /FBS-PSS); (b) Schematic illustration of interactions of the cancer cell membrane with different MNCs. Consistent with Figure 6a, the nonuniform coverage of coronas exposes the positively charged surface regions on MNCs, enabling them to still bind the cancer cells, even for a negative overall zeta potential. All scale bars are 100  $\mu\text{m}$ .

MNCs, forming “soft” protein corona but in a localized fashion, that is not uniformly covering the entire NP. This nonuniformity bears important significance in redistributing the surface electrical charges that directly affect cell binding ability. The results shown in Figure 5 again provide solid experimental evidences on two counts: (1) the cancer cells are indeed negatively charged because of glycolysis and (2) the positively charged NPs are consistently and strongly attracted to the negatively charged cancer cells, while the negatively charged particles are not, making MNCs $\oplus$  a sensitive bioprobe and efficient cell targeting agent.

The fluorescence intensities of the cancer cells, shown in Figure 5a,b, are analyzed by ImageJ software and plotted in Figure 5c. Fluorescence intensity of HeLa cells, bound with MNCs $\oplus$  without FBS treatment, is set as the reference intensity (Figure 5c). Compared to the fluorescence intensity of the HeLa cells, bound with the pure MNCs $\oplus$  as the reference, Figure 5 in fact shows the relative ratios of fluorescence intensity of MNCs $\oplus$  to that of MNCs $\ominus$ . As can be seen in this figure, there is a significant gap between the fluorescent signals between MNCs $\oplus$ - and MNCs $\ominus$ -bound cells. The results are consistent with that shown in Figure 5a,b by the fluorescence microscopy images. According to the data of Figure 5c, there is a 25% decrease in fluorescence intensity from the cancer cell membranes, bound with MNCs $\oplus$  that is decorated with “hard” protein corona. Meanwhile, the fluorescence intensity of cancer cells after incubation with MNCs $\oplus$  in the presence of FBS protein decreases by 28%. The relative fluorescence intensities of the cancer cells bound with MNCs $\ominus$  are extremely low, indicating practically no cell binding regardless of protein corona decoration. As shown in Figure S6, the MNCs–EpcAM binding efficiencies to MCF-7 cells are quite similar before and after 100% FBS treatment.

The electrical change variation of MNCs was investigated as a result protein corona adsorption. The amino groups are prone to protonation, therefore resulting in the electrostatic interaction between cancer cells and MNCs $\oplus$ . These amino groups on the protein-treated MNCs were characterized by colorimetric reaction based on *p*-nitrobenzaldehyde.<sup>36</sup> The amino groups of MNCs $\oplus$  were determined to be 58.4 and 21.4  $\mu\text{mol}\cdot\text{g}^{-1}$ , respectively, before and after formation of protein coronas, while that of MNCs $\ominus$  was 2.7  $\mu\text{mol}\cdot\text{g}^{-1}$ .

These results indicate that 36.7% surface amino groups remained on the MNCs $\oplus$  after 100% FBS treatment. On the basis of these data, one may conclude that there are plenty of surface amino groups remaining for highly efficient cancer cell binding even after 100% FBS treatment. With “hard” protein corona, the MNCs $\oplus$  exhibit improved colloidal stability and bioavailability.

To further investigate the surface-charge-mediated binding of cancer cells by the FBS-treated MNCs $\oplus$ , polystyrene sulfonic (PSS) acid was applied to neutralize the positive regions on MNCs. Table S2 shows the Z-average size and zeta potentials of the treated samples. After treating with PSS at 5, 10, and 20 mg, the diameters of the MNCs increase to 298.3, 325.2, and 315.4 nm, respectively. The corresponding zeta potentials are  $-5.4$ ,  $-22.9$ , and  $-32.6$  mV, respectively.

Figure S7 shows the fluorescence microscopy images of HeLa cells incubated with PSS-treated MNCs. It can be seen that the cancer cell fluorescence is invisible when bound with the PSS-treated MNCs $\oplus$ , indicating neutralization of the positive charges at these PSS concentrations (10 and 20 mg). The consequence of charge neutralization is the elimination of the electrostatic interactions between the cancer cells and MNCs $\oplus$ . Consistently, the zeta potential of the PSS-treated MNCs $\oplus$ /FBS becomes much more negative of  $-49.3$  mV (Table S2).

Figure 6 shows the fluorescence microscope images of HeLa cells binding with different MNCs, namely, MNCs $\oplus$ , 100% FBS-treated MNCs $\oplus$  (MNCs $\oplus$ /FBS), and PSS-treated MNCs $\oplus$ /FBS (MNCs $\oplus$ /FBS-PSS). As shown in this figure, cell binding consistently varies depending upon the surface charge distributions. For MNCs $\oplus$ , as shown in Figure 6a, binding is the strongest as evidenced in the highest fluorescent signal (top row, middle column) for NPs exhibiting a positive zeta potential of +35 mV. Interestingly, significant cell binding remains at a considerable level (see the appreciable fluorescent signal in the second row, middle column of Figure 6a) even for an overall negative zeta potential of  $-14.3$  mV for the FBS-treated MNCs $\oplus$ . This situation is schematically depicted in Figure 6a (second row, right column) that the positively charged particle surface is only nonuniformly covered by the serum protein with the negative charges. However, the entire particle surface is further rendered negative ( $-49.3$  mV) for

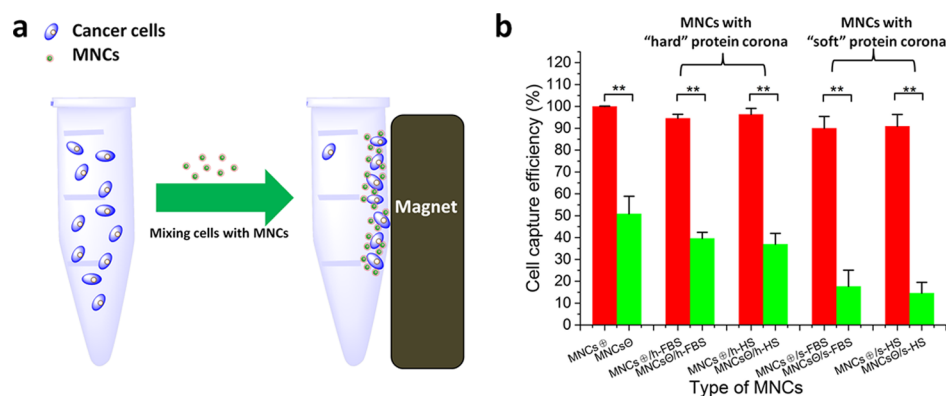


**Figure 7.** (a) Schematic diagram showing charged-based MNCs binding and magnetic separation of the cancer cells; (b) magnetic separation efficiencies of HeLa cells by various surface-functionalized MNCs in PBS solution or in physiological-like environment: “MNCs $\oplus$ ” and “MNCs $\ominus$ ” refer to the MNCs with positive- or negative-surface charges, and their cell capture efficiencies are shown by the red and green bars, respectively. “MNCs $\oplus$ /h-FBS” (red bar) and “MNCs $\ominus$ /h-FBS” (green bar) represent cell capture efficiencies of the positive and negative MNCs, respectively, decorated by the “hard” protein corona. “MNCs $\oplus$ /s-FBS” (red bar) and “MNCs $\ominus$ /s-FBS” (green bar) represent positive and negative MNCs, respectively, decorated by the “soft” protein corona. “MNCs $\oplus$ /h-HS” (red bar) and “MNCs $\ominus$ /h-HS” (green bar) respectively represent the MNCs $\oplus$  and MNCs $\ominus$  with “hard” protein corona from human serum. “MNCs $\oplus$ /s-HS” (red bar) and “MNCs $\ominus$ /s-HS” (green bar) respectively represent the MNCs $\oplus$  and MNCs $\ominus$  with “soft” coronas from human serum.

PSS-treated MNCs (MNCs $\oplus$ /FBS), resulting in the weakest cell binding (no fluorescence). The schematic diagram shown in Figure 6a (bottom row, right column) depicts the surface structure being more uniformly decorated by small negative molecules from PSS.

It should be noted that the sizes of proteins in FBS vary in a wide range. The possible configurations and locations of branched PEI molecules ( $M_w = 10\,000$ ) and adsorbed protein molecules on the MNCs $\oplus$  are schematically shown in Figure 6b. As can be seen in this figure, the positively charged PEI molecules are not entirely and completely covered by the proteins on the particle surface for 100% FBS-treated MNCs $\oplus$ , therefore exposing localized regions that still exhibit the positive charges, effectively available for cell binding.

The abovementioned results are all obtained from the adhered cancer cell binding with various MNCs. We also investigated the various MNC capture efficiencies of the suspended HeLa cells in solution. As schematically depicted in Figure 7a, the suspended HeLa cells can be bound and captured by MNCs and magnetically removed by using a magnet. In Figure 7b, one can see that both MNCs $\oplus$  and MNCs $\ominus$  are capable of capturing cancer cells but with a significantly different efficacy. Figure 7b also shows the MNCs $\oplus$  functionalized with the “hard” or “soft” protein coronas from either FBS or healthy human serum (HS), which show similarly high HeLa cell capture efficiencies, while those of the MNCs $\ominus$  counterparts are much lower. Nonspecific adsorptions take place between the cancer cells and MNCs $\ominus$ , but are gradually suppressed after “hard” and “soft” protein corona treatment compared to that in PBS solution.

To understand the fate of NPs in physiological media, MNCs were designed and developed with different surface structures. In particular, more realistic interfacial conditions were simulated by developing the surface protein coronas on the electrically charged NPs. On the basis of a hallmark characteristic pattern of all cancer cells, metabolically, the high rate of glycolysis and biophysically, a net of negative cell surface charges, the NPs were rendered either positively or negatively charged to target and bind cancer cells (HeLa cells and MCF-7 cells) through electrostatic interactions. In a

parallel study, biomarkers (anti-EpCAM antibody) were also used for cancer cell targeting and binding via immunological reactions.

The marker-based targeting was required to perform at 37 °C for 60 min because of slow reaction kinetics, while the charge-driven cell binding was not only much stronger but completed at a significantly faster rate within 5 min, even at a low temperature of 4 °C. Fluorescence microscopy images showed efficient HeLa cell binding by positively charged NPs at 4 °C for 5 min. However, biomarker-based binding by MNCs–EpCAM appeared to be diffused at 37 °C for 60 min. This sharp contrast provides a strong experimental evidence for much stronger nano/cell interfacial electrostatic binding compared to the biomarker-based immunological interactions.

To simulate real physiological fluids, such as blood plasma, protein coronas are decorated on the surface-charged NPs, resulting in changes in the zeta potential and hydrodynamic size, as shown in Figure 6. As can be clearly seen in Figure 6a, the undecorated MNCs $\oplus$  are capable of strong cell binding for its positive charges (+32.3 mV), manifested by the strongest fluorescence (first row, middle column). The positively charged surface of MNCs $\oplus$  can be effectively modified by 100 v/v % of FBS, rendering the particle surface partially covered by proteins with negative charges. As a result, the average zeta potential is varied from a positive +32.3 mV to a negative –14.3 mV. However, because the protein coverage is nonuniform, some of the positively charged regions on the particle still appear to be locally positive and responsible for considerable cell binding as shown in the fluorescent image of Figure 6a (second row, middle column). This is an important finding of this study that a “negatively charged corona” can be created for effective cell targeting, binding, and magnetic separation, even in a physiological environment. Targeting, binding, and magnetic capture of the spiked cancer cells, suspended in healthy human serum, was also achieved by MNCs $\oplus$  or MNCs $\ominus$ . This experimental evidence proved the feasibility of cancer cell capture via electrostatic interactions between the oppositely charged MNCs and negatively charged cancer cells.

On top of MNCs $\oplus$ /FBS (i.e., MNCs treated with FBS), the NPs are treated with PSS aqueous solution (20 mg·mL<sup>-1</sup>) for further surface charge modification (MNCs $\oplus$ /FBS-PSS). In this situation, the surface corona structure is characterized by small negative molecules from PSS that can effectively neutralize the positive charges that remain on MNCs $\oplus$ /FBS, leading to an even more negative zeta potential of -49.3 mV. As shown in Figure 6a (third row and middle column), no fluorescence can be observed, indicating significantly reduced electrostatic interactions between MNCs and HeLa cells.

Electrostatic interactions of MNCs with the cell membrane are schematically shown in Figure 6b. As shown in this figure, the electrostatic interaction strength varies according to the surface functionalization and corona structures. MNCs $\oplus$  are composed of an unaltered positive particle surface therefore possess the strongest attraction to cell membrane. Although modulated by surface corona with a negative zeta potential, MNCs $\oplus$ /FBS remains effective in cell binding because of locally distributed positive charges on the particle surface. As shown in Figure 6, both MNCs $\oplus$  and MNCs $\oplus$ /FBS are capable of cell binding and targeting, but the latter functions in a biologically more realistic situation, namely, physiological environment. As described in the Introduction, NPs encounter much more complicated biological systems when dispersed in blood plasma. Therefore, it is critical to understand the nano-bio interfaces in terms of the intended functions, such as cell targeting and drug delivery, especially when the nano vectors are decorated by various proteins. As shown in this study, the surface charges of NPs can be effectively modified by adsorption of protein corona depending on the FBS concentration. Both "hard" and "soft" protein coronas are utilized to modulate the charge distributions of NPs in order to control effective cell binding by the MNCs $\oplus$ .

## CONCLUSIONS

In summary, magnetic NPs have been developed in two different manners: one conjugated with biomarkers and the other surface-functionalized to exhibit electrical charges; both are investigated for the effects of nano-bio interfaces on effective cell targeting and binding. Specifically, the biomarker-based particles are labeled with anti-EpCAM antibody and applied to cell targeting of epithelium HeLa and MCF-7 cell lines. The charge-driven NPs are functionalized either by silica for negative charges or PEI for positive changes. While both exhibit considerable cell binding, the charge-driven cell binding is shown to be comparably much stronger even in a physiological environment.

To investigate cell binding in a simulated a physiological system, the functionalized NPs mentioned above are decorated with various protein coronas. The charge-based particles show strong electrostatic interactions with cancer cells even with surface-decorated protein coronas. Furthermore, the cell targeting ability is not significantly affected by zeta potential being reversed from positive to negative via corona decoration. Because the particle surface is not entirely covered by corona, the positively charged regions are exposed, majorly responsible for strong cell binding. The charge-mediated cancer cell targeting remains effective regardless of the biomarker proteins being under- or overexpressed. By FBS protein adsorption, cytotoxicity and colloidal stability of the electrically charged NPs are well improved. On the basis of this new principle, positively charged magnetic NPs with corona decoration may

achieve sensitive CTC detection in the physiological environment (Figure 7).

## EXPERIMENTAL SECTION

**Materials.** Iron(III) chloride hydrate (FeCl<sub>3</sub>·6H<sub>2</sub>O), ethylene glycol, sodium acetate, sodium acetate, hydrochloric acid (37 wt % aqueous solution), ammonium hydroxide (NH<sub>4</sub>OH, 28 wt %), and *N,N*-dimethyl formamide (DMF) were purchased from Shanghai (China) Reagent Company. Tetraethyl orthosilicate (TEOS), FITC, (3-aminopropyl)triethoxysilane (APTES), and anti-EpCAM antibody (SAB 4700423) were purchased from Sigma-Aldrich (USA). Branched PEI (99%, *M<sub>w</sub>* = 10 000) and PSS were purchased from Alfa Aesar. Rhodamine-phalloidin and DAPI were purchased from Shanghai Yeasen Biotech Co, Ltd. DIW (18.2 MΩ·cm resistivity at 25 °C) was acquired by using a Thermo Easypure II UF System throughout the entire experiment.

**Methods.** Cell culture materials RPMI-1640 medium, penicillin-streptomycin, and 0.25% trypsin-ethylenediaminetetraacetic acid were purchased from Gibco Corp. PBS and DMEM were purchased from Hyclone Corp. Heat-inactivated FBS were purchased from MRC Corp. The rest of media for cell culture was purchased from NEST Corp.

For the synthesis of surface-charged and protein corona-coated magnetic composite NPs (MNCs), MNCs were synthesized by a facile modified hydrothermal reaction according to our previous work.<sup>31</sup> In a typical process, 0.81 g of FeCl<sub>3</sub>·6H<sub>2</sub>O, 0.3 g of polyacrylic acid, and 1.8 g of urea were dissolved in 30 mL of ethylene glycol under ultrasonication. Stirred for 0.5 h, the clear solution was transferred into a Teflon-lined stainless-steel autoclave. The autoclave was heated to 200 °C and maintained at this temperature for 12 h. When cooled to room temperature, a black product, namely Fe<sub>3</sub>O<sub>4</sub> microspheres, was collected and washed with ethanol and DIW for three times.<sup>37</sup>

Fe<sub>3</sub>O<sub>4</sub>@SiO<sub>2</sub> composite NPs were prepared by a sol-gel reaction.<sup>38</sup> The Fe<sub>3</sub>O<sub>4</sub> microspheres were treated in 0.10 M HCl aqueous solution under sonication for 15 min and repeatedly magnetically separated and redispersed in DIW for 6 times until neutral. The Fe<sub>3</sub>O<sub>4</sub> microspheres were coated with silica via hydrolysis and condensation of TEOS. In a typical synthesis, 83.7 g of ethyl alcohol and 26.8 g of DIW (v/v = 80:20) were added to flask with three necks under mechanical stirring. Ammonium hydroxide was added to flask adjusting pH to 10, and 150 mg of Fe<sub>3</sub>O<sub>4</sub> microspheres was then dispersed in the mixed solution under sonication. After stirring and sonication for 0.5 h, 80 μL of TEOS was added into the reaction system and maintained for 24 h. The product was collected for several times of washing with ethanol and DIW and stored at 4 °C for use.

To label MNCs $\ominus$  with fluorescent dye, 1 mL of ethanol solution with the APTES-FITC complex (5 μL of APTES and 1.5 mg of FITC were reacted under dark conditions overnight in 2.5 mL of ethanol) was mixed with Fe<sub>3</sub>O<sub>4</sub>@SiO<sub>2</sub> microspheres in the mixture solvent of 45 mL of ethanol and 5 mL of DIW. NH<sub>4</sub>OH was used to adjust solution pH to 10. To obtain the fluorescent microspheres with negative surface charges, 60 μL of TEOS was added into the APTES-FITC complex and reacted for 4 h. The reaction lasted for another 20 h in the dark. Upon washing, the negatively charged fluorescent MNC particles (MNCs $\ominus$ ) were prepared.

The MNCs $\oplus$  particles were synthesized by surface modifying MNCs $\ominus$  with PEI. In a typical synthesis, 20 mg of MNCs $\ominus$  and 20 mg of PEI were dissolved in 25 mL of methanol by ultrasonication. The mixture was stirred under ultrasonication in darkness for 2 h, and MNCs $\oplus$  with fluorescence were collected and washed with ethanol and DIW.

For the synthesis of carboxyl group-functionalized magnetic composite NPs (MNCs-COOH) and conjugation with anti-EpCAM antibody, a two-step process was applied to the synthesis of MNCs-COOH using Fe<sub>3</sub>O<sub>4</sub>@SiO<sub>2</sub> as a substrate. MNCs were functionalized with the amino group (NH<sub>2</sub>-MNCs). Fe<sub>3</sub>O<sub>4</sub>@SiO<sub>2</sub> nanospheres (20 mg) were dispersed in a mixture of DIW and ethanol, and with 60 μL

of APTES added for the reaction system. The mixture was stirred at room temperature for 1 h and heated at 80 °C for 2 h. NH<sub>2</sub>-MNCs were obtained after a washing process with ethanol and DIW. To prepare COOH-MNCs, 20 mg of NH<sub>2</sub>-MNCs and 15 mg of succinic anhydride were dissolved in 56 g of DMF. Stirred for 24 h, COOH-MNCs were collected and washed with ethanol and DIW each for three times.

Anti-EpCAM antibody-conjugated MNCs (MNCs–EpCAM) was obtained through a chemical reaction between the amino groups of antibody and the carboxylic groups on the surfaces of MNCs, mediated by EDC and NHS esters. MNCs (1 mg) and 50 μg of antibody were used in this process. Antibody-conjugated MNCs were stored in PBS (pH 7.4), embodying 1 wt % BSA and NaN<sub>3</sub> until use. To confirm successful conjugation, chromatography strips fixed with rabbit-anti-mouse IgG in C-line were used. MNCs (2 μg) were dipped onto each strip for observation by naked eyes.

For preparation of protein-corona-coated MNCs, 1 mg of surface-charged or antibody-conjugated MNCs were incubated in 1 mL of DMEM media with varied concentrations of FBS: 0, 10, 50, and 100 v/v % for 1 h at 25 °C. The NPs were then washed three times with DMEM media to obtain protein corona-coated MNCs for cancer cell binding, and the remaining protein coronas after the washing process were called “hard” protein corona.<sup>33</sup> The interaction between cancer cells and MNCs in the media of 100% FBS are defined as cancer cell binding by the “soft” protein corona-coated MNCs. The “hard” and “soft” protein corona-coated MNCs are denoted as MNCs/h-FBS and MNCs/s-FBS, respectively.

For preparation of PSS-modified MNCs⊕/h-FBS and MNCs⊕, 1 mg of MNCs⊕/h-FBS (“hard” protein corona-coated MNCs) and MNCs⊕ particles was incubated in 1 mL of PSS aqueous solution (20 mg·mL<sup>-1</sup>) at 25 °C for 1 h. These NPs were washed with DIW for three times and denoted as PSS-modified “hard” protein corona-coated MNCs (MNCs⊕/FBS-PSS) and PSS-modified MNCs⊕ (MNCs⊕/PSS), respectively.

**Characterization of MNCs.** DLS measurements were carried out at 298.0 K using Zetasizer Nano-ZS (Malvern, UK) equipped with standard 633 nm laser. JEM-2010 TEM and JEOL S4800 scanning electron microscopy were used to characterize the morphology of MNCs. The HAADF-STEM image and element mapping were obtained by Titan Themis 60-300 G2. (Thermo Fisher Scientific, USA) TG analysis data were obtained with a Pyris-1 (PerkinElmer, USA) thermal analysis system under a nitrogen atmosphere at a heating rate of 10 °C·min<sup>-1</sup> from room temperature to 800 °C.

**Cell Lines and Culture Conditions.** HeLa cells (human cervical cancer cells) were cultured in DMEM. MCF-7 cells (human breast cancer cells) were cultured in RPMI 1640 medium. Both were supplemented with 1% penicillin–streptomycin and 10% FBS. All cells in a humidified atmosphere contained 5% CO<sub>2</sub> at 37 °C. Depending on the experiment, cells were seeded on 6-well, 24-well, 96-well plates, confocal dish, or 25 cm<sup>2</sup> flasks. All sterile plastics were sourced from NEST Corp.

**Fluorescence Microscopy Images.** Cells were seeded on 24-well plates and incubated for 24 h. After incubation with MNCs at 37 or 4 °C for different times, the plates were washed with PBS by blowing using a pipette for three times. Cells and MNCs were observed and analyzed under a Nikon ECLIPSE Ti Inverted Fluorescence Microscope.

**Confocal Microscopy Imaging.** HeLa and MCF-7 cells were plated on a confocal dish for 24 h. Upon incubation with MNCs (0.2 mg·mL<sup>-1</sup>) for 5 min at 4 °C, the culture medium was removed and samples were washed with PBS three times. The cell nucleus and the cell membrane were stained with DAPI and rhodamine–phalloidin, respectively. MNCs were labeled with FITC. Cells and MNCs were observed and analyzed with a Leica TCS SPS Confocal microscope.

**SDS-PAGE and LC/Tandem MS Characterization.** MNCs were incubated in 1 mL of DMEM media with different FBS concentrations of 0, 10, 50, and 100% (v/v) at 25 °C for 1 h. MNCs were then washed with PBS buffer three times to obtain the protein corona-coated MNCs. The adsorbed proteins were stripped from MNCs by adding the NuPAGE LDS sample loading buffer and

heated at 95 °C for 10 min. The eluted proteins were transferred to a new tube. The disulfide bonds in proteins were cleaved using a reducing agent (50 mM dithiothreitol) and heated at 95 °C for 10 min. The samples were then loaded on gel and run at 110 V for 90 min. Each gel included one lane of a standard molecular weight ladder, and 100% of FBS-conducted gel was excised from PAGE. The proteins were digested with trypsin, and the resulting peptides were separated by capillary LC/tandem MS (LC–MS/MS) using ES1-QUAD-TOF (Boyuan Biotech, Shanghai). The peptides were identified using the NCBI protein database for *Bos taurus*.

**Suspended HeLa Cells Capturing by Different MNCs.** HeLa cells (5 × 10<sup>5</sup>) were suspended in 1 mL of PBS, FBS, or healthy human serum, and 0.2 mg of MNCs was added to the cell suspension and incubated at 4 °C for 5 min with gentle agitation. After incubation, the MNC-bound cells were captured by a permanent magnet, and free cells were removed by washing with PBS for three times. The captured cancer cells were released by removing the magnet and resuspended in PBS. The cells were counted by a hemocytometer (XB-K-25, QIJING Co. Ltd, Shanghai).

## ■ ASSOCIATED CONTENT

### 📄 Supporting Information

The Supporting Information is available free of charge on the ACS Publications website at DOI: 10.1021/acsami.8b15098.

Cell viability of cells treated by different NPs; fluorescent microscopy images of fluorescence dye FITC-labeled magnetic NPs and fluorescent signal stability; photographs of lateral flow strips with IgG anti-antibody fixed in C-line and dipped with different kinds of MNCs; fluorescence confocal images of HeLa and MCF-7 cells treated by different MNCs; fluorescence microscopy images and corresponding quantitative intensity of the HeLa cells incubated with different MNCs and fluorescence confocal images of HeLa cells incubated with surface-charged NPs; proteins identified in the protein coronas on the positively and negatively charged MNCs after 100% FBS treatment; fluorescence microscopy images of MCF-7 cells incubated with different NPs; DLS size and zeta potentials of different MNCs; and fluorescence microscopy images of HeLa cell incubated with the positively charged MNCs treated by different amounts of PSS (PDF)

## ■ AUTHOR INFORMATION

### Corresponding Authors

\*E-mail: [enjoysimplife@163.com](mailto:enjoysimplife@163.com) (J.Z.).

\*E-mail: [donglu.shi@uc.edu](mailto:donglu.shi@uc.edu) (D.S.).

\*E-mail: [yilongwang@tongji.edu.cn](mailto:yilongwang@tongji.edu.cn) (Y.W.).

### ORCID

Donglu Shi: 0000-0002-0837-7780

### Author Contributions

<sup>†</sup>J.Z. and S.W. contributed equally to this work.

### Notes

The authors declare no competing financial interest.

## ■ ACKNOWLEDGMENTS

This work was supported by grants from the National Natural Science Foundation of China (31571018) and the Fundamental Research Funds for the Central Universities (22120170166). The work was partially funded by the Natural Science Foundation of China (51873096), Natural Science Foundation of Shandong Province (ZR201807060363), and

Primary Research & Development Plan of Shandong Province (2017GGX20132).

## ■ ABBREVIATIONS

MNCs, magnetic nanocomposite particles  
MNCs $\oplus$ , positively-charged magnetic nanocomposite particles  
MNCs $\ominus$ , negatively-charged magnetic nanocomposite particles  
RES, reticuloendothelial system  
CTC, circulating tumor cells  
ATP, adenosine triphosphate  
TCA, tricarboxylic acid  
EpCAM, epithelial cell adhesion molecule  
COOH-MNCs, carboxylated magnetic nanocomposite particles  
NH<sub>2</sub>-MNCs, magnetic nano composites with surface amino groups  
MNCs-EpCAM, anti-EpCAM antibody conjugated magnetic nanocomposite particles  
MNCs-BSA, BSA conjugated magnetic nanocomposite particles  
DAPI, 4',6-diamidino-2-phenylindole  
FBS, fetal bovine serum  
DMEM, Dulbecco's modified Eagle's medium  
PBS, phosphate-buffered saline  
MNCs/h-FBS, "hard" protein coronas-coated MNCs  
MNCs/s-FBS, "soft" protein corona-coated MNCs  
MNCs $\oplus$ /FBS-PSS, PSS modified "hard" protein corona-coated MNCs  
MNCs $\oplus$ /PSS, PSS modified positively-charged MNCs

## ■ REFERENCES

- (1) Monopoli, M. P.; Åberg, C.; Salvati, A.; Dawson, K. A. Biomolecular Coronas Provide the Biological Identity of Nanosized Materials. *Nat. Nanotechnol.* **2012**, *7*, 779–786.
- (2) Nguyen, V. H.; Lee, B.-J. Protein Corona: A New Approach for Nanomedicine Design. *Int. J. Nanomed.* **2017**, *12*, 3137–3151.
- (3) Mahmoudi, M. Debugging Nano–Bio Interfaces: Systematic Strategies to Accelerate Clinical Translation of Nanotechnologies. *Trends Biotechnol.* **2018**, *36*, 755–769.
- (4) Walkey, C. D.; Olsen, J. B.; Guo, H.; Emili, A.; Chan, W. C. W. Nanoparticle Size and Surface Chemistry Determine Serum Protein Adsorption and Macrophage Uptake. *J. Am. Chem. Soc.* **2012**, *134*, 2139–2147.
- (5) Capriotti, A. L.; Caracciolo, G.; Caruso, G.; Foglia, P.; Pozzi, D.; Samperi, R.; Laganà, A. Differential analysis of "protein corona" profile adsorbed onto different nonviral gene delivery systems. *Anal. Biochem.* **2011**, *419*, 180–189.
- (6) Boyer, C.; Whittaker, M. R.; Bulmus, V.; Liu, J.; Davis, T. P. The Design and Utility of Polymer-stabilized Iron-Oxide Nanoparticles for Nanomedicine Applications. *NPG Asia Mater.* **2010**, *2*, 23–30.
- (7) Du, X.; Zhou, J.; Wu, L.; Sun, S.; Xu, B. Enzymatic Transformation of Phosphate Decorated Magnetic Nanoparticles for Selectively Sorting and Inhibiting Cancer Cells. *Bioconjugate Chem.* **2014**, *25*, 2129–2133.
- (8) Bhunia, A. K.; Samanta, P. K.; Aich, D.; Saha, S.; Kamilya, T. Biocompatibility Study of Protein Capped and Uncapped Silver Nanoparticles on Human Hemoglobin. *J. Phys. D: Appl. Phys.* **2015**, *48*, 235305.
- (9) Barrán-Berdón, A. L.; Pozzi, D.; Caracciolo, G.; Capriotti, A. L.; Caruso, G.; Cavaliere, C.; Riccioli, A.; Palchetti, S.; Laganà, A. Time Evolution of Nanoparticle-Protein Corona in Human Plasma: Relevance for Targeted Drug Delivery. *Langmuir* **2013**, *29*, 6485–6494.
- (10) Duan, X.; Li, Y. Physicochemical Characteristics of Nanoparticles Affect Circulation, Biodistribution, Cellular Internalization, and Trafficking. *Small* **2013**, *9*, 1521–1532.
- (11) Xiao, K.; Li, Y.; Luo, J.; Lee, J. S.; Xiao, W.; Gonik, A. M.; Agarwal, R. G.; Lam, K. S. The Effect of Surface Charge on in Vivo Biodistribution of PEG-oligocholeic Acid Based Micellar Nanoparticles. *Biomaterials* **2011**, *32*, 3435–3446.
- (12) Xu, F.; Yuan, Y.; Shan, X.; Liu, C.; Tao, X.; Sheng, Y.; Zhou, H. Long-Circulation of Hemoglobin-Loaded Polymeric Nanoparticles as Oxygen Carriers with Modulated Surface Charges. *Int. J. Pharm.* **2009**, *377*, 199–206.
- (13) Yue, Z.-G.; Wei, W.; Lv, P.-P.; Yue, H.; Wang, L.-Y.; Su, Z.-G.; Ma, G.-H. Surface Charge Affects Cellular Uptake and Intracellular Trafficking of Chitosan-based Nanoparticles. *Biomacromolecules* **2011**, *12*, 2440–2446.
- (14) Dash, B. C.; Réthoré, G.; Monaghan, M.; Fitzgerald, K.; Gallagher, W.; Pandit, A. The Influence of Size and Charge of Chitosan/Polyglutamic Acid Hollow Spheres on Cellular Internalization, Viability and Blood Compatibility. *Biomaterials* **2010**, *31*, 8188–8197.
- (15) He, C.; Hu, Y.; Yin, L.; Tang, C.; Yin, C. Effects of Particle Size and Surface Charge on Cellular Uptake and Biodistribution of Polymeric Nanoparticles. *Biomaterials* **2010**, *31*, 3657–3666.
- (16) Du, J.-Z.; Du, X.-J.; Mao, C.-Q.; Wang, J. Tailor-made Dual pH-sensitive Polymer-Doxorubicin Nanoparticles for Efficient Anti-cancer Drug Delivery. *J. Am. Chem. Soc.* **2011**, *133*, 17560–17563.
- (17) Li, J.; Yu, X.; Wang, Y.; Yuan, Y.; Xiao, H.; Cheng, D.; Shuai, X. A Reduction and pH Dual-sensitive Polymeric Vector for Long-circulating and Tumor-targeted siRNA Delivery. *Adv. Mater.* **2014**, *26*, 8217–8224.
- (18) Chen, J.; Ding, J.; Wang, Y.; Cheng, J.; Ji, S.; Zhuang, X.; Chen, X. Sequentially Responsive Shell-Stacked Nanoparticles for Deep Penetration into Solid Tumors. *Adv. Mater.* **2017**, *29*, 1701170.
- (19) Dai, Q.; Yan, Y.; Ang, C.-S.; Kempe, K.; Kamphuis, M. M. J.; Dodds, S. J.; Caruso, F. Monoclonal Antibody-Functionalized Multilayered Particles: Targeting Cancer Cells in the Presence of Protein Coronas. *ACS Nano* **2015**, *9*, 2876–2885.
- (20) Weiner, L. M.; Surana, R.; Wang, S. Monoclonal Antibodies: Versatile Platforms for Cancer Immunotherapy. *Nat. Rev. Immunol.* **2010**, *10*, 317–327.
- (21) Cerchia, L.; de Franciscis, V. Targeting Cancer Cells with Nucleic Acid Aptamers. *Trends Biotechnol.* **2010**, *28*, 517–525.
- (22) Wang, S.; Huang, P.; Chen, X. Hierarchical Targeting Strategy for Enhanced Tumor Tissue Accumulation/Retention and Cellular Internalization. *Adv. Mater.* **2016**, *28*, 7340–7364.
- (23) Svensen, N.; Walton, J. G. A.; Bradley, M. Peptides for Cell-selective Drug Delivery. *Trends Pharmacol. Sci.* **2012**, *33*, 186–192.
- (24) Blanco, E.; Shen, H.; Ferrari, M. Principles of Nanoparticle Design for Overcoming Biological Barriers to Drug Delivery. *Nat. Biotechnol.* **2015**, *33*, 941–951.
- (25) Tan, S. J.; Lakshmi, R. L.; Chen, P.; Lim, W. T.; Yobas, L.; Lim, C. T. Versatile Label Free Biochip for the Detection of Circulating Tumor Cells from Peripheral Blood in Cancer Patients. *Biosens. Bioelectron.* **2010**, *26*, 1701–1705.
- (26) Hou, H. W.; Warkiani, M. E.; Khoo, B. L.; Li, Z. R.; Soo, R. A.; Tan, S. W.; Lim, W. T.; Han, J.; Bhagat, A. A. S.; Lim, C. T. Isolation and Retrieval of Circulating Tumor Cells Using Centrifugal Forces. *Sci. Rep.* **2012**, *3*, 1259.
- (27) Chen, B.; Le, W.; Wang, Y.; Li, Z.; Wang, D.; Ren, L.; Lin, L.; Cui, S.; Hu, J. J.; Hu, Y.; Yang, P.; Ewing, R. C.; Shi, D.; Cui, Z. Targeting Negative Surface Charges of Cancer Cells by Multifunctional Nanoparticles. *Theranostics* **2016**, *6*, 1887–1898.
- (28) Warburg, O.; Wind, F.; Negelein, E. The Metabolism of Tumors in the Body. *J. Gen. Physiol.* **1927**, *8*, 519–530.
- (29) Pavlova, N. N.; Thompson, C. B. The Emerging Hallmarks of Cancer Metabolism. *Cell Metab.* **2016**, *23*, 27–47.
- (30) Luc, R.; Tortorella, S. M.; Ververis, K.; Karagiannis, T. C. Lactate as an Insidious Metabolite due to the Warburg Effect. *Mol. Biol. Rep.* **2015**, *42*, 835–840.

(31) Han, X.; Deng, Z.; Yang, Z.; Wang, Y.; Zhu, H.; Chen, B.; Cui, Z.; Ewing, R. C.; Shi, D. Biomarkerless Targeting and Photothermal Cancer Cell Killing by Surface-electrically-charged Superparamagnetic Fe<sub>3</sub>O<sub>4</sub> Composite Nanoparticles. *Nanoscale* **2017**, *9*, 1457–1465.

(32) Du, J.; Zhao, Y.; Yang, Z.; Xu, C.; Lu, Y.; Pan, Y.; Shi, D.; Wang, Y. Influence of Controlled Surface Functionalization of Magnetic Nanocomposites on the Detection Performance of Immunochromatographic test. *Sens. Actuators, B* **2016**, *237*, 817–825.

(33) Maffre, P.; Nienhaus, K.; Amin, F.; Parak, W. J.; Nienhaus, G. U. Characterization of Protein Adsorption onto FePt Nanoparticles using Dual-focus Fluorescence Correlation Spectroscopy. *Beilstein J. Nanotechnol.* **2011**, *2*, 374–383.

(34) Hühn, D.; Kantner, K.; Geidel, C.; Brandholt, S.; De Cock, I.; Soenen, S. J. H.; Rivera-Gil, P.; Montenegro, J.-M.; Braeckmans, K.; Müllen, K.; Nienhaus, G. U.; Klapper, M.; Parak, W. J. Polymer-Coated Nanoparticles Interacting with Proteins and Cells: Focusing on the Sign of the Net Charge. *ACS Nano* **2013**, *7*, 3253–3263.

(35) Bruce, I. J.; Sen, T. Surface Modification of Magnetic Nanoparticles with Alkoxysilanes and Their Application in Magnetic Bioseparations. *Langmuir* **2005**, *21*, 7029–7035.

(36) Xu, X.; Deng, C.; Gao, M.; Yu, W.; Yang, P.; Zhang, X. Synthesis of Magnetic Microspheres with Immobilized Metal Ions for Enrichment and Direct Determination of Phosphopeptides by Matrix-Assisted Laser Desorption Ionization Mass Spectrometry. *Adv. Mater.* **2006**, *18*, 3289–3293.

(37) Xu, F.; Cheng, C.; Chen, D.-X.; Gu, H. Magnetite Nanocrystal Clusters with Ultra-high Sensitivity in Magnetic Resonance Imaging. *ChemPhysChem* **2012**, *13*, 336–341.

(38) Kokkinopoulou, M.; Simon, J.; Landfester, K.; Mailänder, V.; Lieberwirth, I. Visualization of the Protein Corona: Towards a Biomolecular Understanding of Nanoparticle-cell-interactions. *Nanoscale* **2017**, *9*, 8858–8870.